Radially Classified Aerosol Detector for Aircraft-Based Submicron Aerosol Measurements

LYNN M. RUSSELL, SHOU-HUA ZHANG, RICHARD C. FLAGAN, AND JOHN H. SEINFELD

Department of Chemical Engineering, California Institute of Technology, Pasadena, California

MARK R. STOLZENBURG

Aerosol Dynamics, Inc., Berkeley, California

ROBERT CALDOW

TSI, Inc., St. Paul, Minnesota

(Manuscript received 27 April 1995, in final form 29 September 1995)

ABSTRACT

A radially classified aerosol detector (RCAD) for fast characterization of fine particle size distributions aboard aircraft has been designed and implemented. The measurement system includes a radial differential mobility analyzer and a high-flow, high-efficiency condensation nuclei counter based on modifications to a commercial model (TSI, model 3010). Variations in pressure encountered during changes in altitude in flight are compensated by feedback control of volumetric flow rates with a damped proportional control algorithm. Sampling resolution is optimized with the use of an automated dual-bag sampling system. This new system has been tested aboard the University of Washington C131a research aircraft to demonstrate its in-flight performance capabilities. The system was used to make measurements of aerosol, providing observations of the spatial variability within the cloud-topped boundary layer off the coast of Monterey, California.

1. Introduction

A primary need in atmospheric research instrumentation is the capability to perform high-resolution, in situ aerosol measurements from aircraft and ships to probe the spatial and temporal variability of the tropospheric aerosol (Daum and Springston 1993). A striking example of the effect of spatial variability of aerosol characteristics on cloud properties is provided by so-called ship tracks first observed from satellites (Conover 1966) and later from aircraft measurements (Radke et al. 1989; King et al. 1993). Ship tracks provide a dramatic example of the interaction between aerosol features and resulting cloud characteristics; measuring this microphysical evolution by means of in situ measurements was an important goal of the Monterey Area Ship Track (MAST) Experiment. These spatially well-defined perturbations of the aerosol concentration and composition and of cloud properties provide an opportunity to study the broader question of the impact of anthropogenic emissions on cloud properties.

Theoretical studies have predicted that both marine and anthropogenically influenced tropospheric aerosols should vary diurnally as a result of photochemical reactions resulting in secondary new particle formation and aerosol growth (Russell et al. 1994). Such work suggests that the aerosol size distribution will evolve during the day through a series of characteristic size distributions indicative of periods of nucleation and condensation. Providing in situ evidence for such direct dependence of aerosol properties on other atmospheric variables suggests studies of marine boundary layer and free-tropospheric aerosol with aircraft instrumented to measure size distributions quickly and automatically.

In order to characterize small-scale or ephemeral features in the atmospheric aerosol, airborne measurements of submicron aerosol size distributions at a frequency capable of resolving the differences, for example, between the cloud line features and surrounding clouds are required. Commercially available submicron aerosol classification and counter designs are not suited for this application because of the long sampling times required to characterize two or more decades of the submicron size distribution. We describe here the design and implementation of a new system for aircraft-based sampling of tropospheric aerosol.

2. Aircraft-based aerosol measurements

Aircraft-based aerosol measurements with optical particle counters aboard aircraft have provided valu-

Corresponding author address: Prof. John H. Seinfeld, Division of Engineering and Applied Science, California Institute of Technology, 104-44, Pasadena, CA 91125.

able insight into the variation of aerosol with altitude and the character of aerosol in and above cloud (Clarke 1991; Hegg 1993; Radke et al. 1989; King et al. 1993). Radke et al. (1989) described a system for obtaining size distribution information with an optical particle counter (OPC) for particles greater than 0.1-μm diameter. Clarke et al. (1991) introduced the thermo-optical aerosol detector (TOAD) to characterize both the dry aerosol distribution and its volatility. Hegg et al. (1993) and Clarke (1993) have extended the effective size range of aerosol measurement using mobility-classification to below 20-nm diameter.

Several constraints are inherent to aircraft-based submicron aerosol measurement, including limitations on size, weight, and power, as well as the necessity for making fast measurements while adjusting rapidly for changing pressure, temperature, and humidity conditions. Previous investigations measuring submicron aerosol from aircraft are listed in Table 1. The need for rapid measurements derives from the aircraft's speed relative to the spatial scale of changes in aerosol properties. The spatial resolution possible with an airborne instrument is determined both by the speed of the instrument and the speed of the aircraft. Conventional differential mobility analyzer analysis requires a sampling period of about 10 min. If continuous sampling methods were employed, the resulting size distribution would represent, for example, at a speed of 100 m s^{-1}, a composite distribution of sized aerosol concentrations for a 60-km flight leg. Since airmass characteristics can change drastically over 60 km, several groups have employed a grab sampling approach in which air is drawn into a holding chamber and stored while a single measurement is processed (Radke et al. 1989; Hegg et al. 1993; Clarke 1993). Radke et al. (1989) employed a 90-L steel cylindrical chamber with a floating piston filled by ram pressure to store the aerosol for size classification and were thus able to store a sample collected in about 5 s. Hegg et al. (1993) also employed a large (2.5 m^3) polyethylene bag for analysis over a 10-min period of size classification.

The approach of grab sampling has successfully provided in-flight snapshots of aerosol in air masses, which have been coupled with continuous condensation nuclei (CN) measurements to determine the aerosol's spatial variability. Measurement speed still limits both the frequency with which complete distributions can be acquired and the instrument's lower detection limit. Diffusional deposition of aerosol particles on the walls of a sampling vessel can reduce the number concentrations dramatically for long counting times (Fuchs 1964; Crump and Seinfeld 1981). Consequently, the chamber's volume must be chosen such that particle losses during sampling and analysis are minimized. Particle losses in a chamber are also exacerbated by electrostatic enhancement of charged particles on the chamber walls (McMurry and Rader 1985). Hegg et al. (1993) measured ultrafine particles during a 10-min sample measurement protocol by employing a 2.5-m^3 chamber.

The speed with which aerosol size distributions may be characterized is limited by the time required to obtain significant particle counts for each size channel, which, for a given ambient concentration, is a function of the counting statistics and efficiency of the detector and the flow profile in the measurement system (Wang and Flagan 1990; Russell et al. 1995). In single-particle counting operation, the counting statistics of condensation particle counters (CPCs) are governed by the number of particles that can be counted in a specified time interval. For a stream of air containing N_i particles (cm^{-3}) with flow rate Q_s at the detector and detection efficiency $s(D_p, \nu)$ for particles of diameter D_p and charge ν, for channel i the signal measured (S_i) is proportional to their product, $N_i Q_s s(D_p, \nu)$.

Of commercially available counters, the TSI 3025 has the highest detection efficiency for ultrafine (less than 10-nm diameter) particles (Stolzenburg and McMurry 1989; Quant et al. 1992). However, in order to obtain uniform saturation the sample flow is surrounded by a sheath flow that dilutes the flow to the counter of 0.3 L min^{-1} by a factor of 10, so that Q_s is 0.03 L min^{-1}. Other counters, in particular TSI models 3010 and 3022, have detector flow rates of 1 L min^{-1} but have 50% detection efficiency cutoffs of 10 and 8 nm, respectively, such that size distributions may not be extended to the ultrafine range (Quant et al. 1992).

Airborne measurements of particle size distributions by differential mobility analysis are further complicated by pressure variations that accompany altitude

TABLE 1. Comparison of ranges, sampling times, and control methods of aircraft instrumentation for measuring size-classified submicron aerosol particles. The characteristics contained in the table are based on published descriptions from Brock et al. (1989), Hudson and Clarke (1992), Hegg et al. (1993), Frick and Hoppel (1993), and the present work.

Reference	Platform	Diameter range	Instrument	Sampling time
Brock et al. (1989)	UW C131a	0.010–1.0 μm	Electrostatic aerosol analyzer (TSI) Diffusion battery (TSI)	Not specified
Hegg et al. (1993)	UW C131a	0.020–0.6 μm	Differential mobility analyzer (TSI)	4 min
Frick and Hoppel (1993)	NRL Airship	0.010–1.2 μm	Differential mobility analyzer (NRL)	10 min
Hudson and Clarke (1992)	NCAR Electra	0.020–0.6 μm	Differential mobility analyzer (TSI)	Not specified
This work	UW C131a	0.005–0.2 μm	Differential mobility analyzer (CIT)	45 s

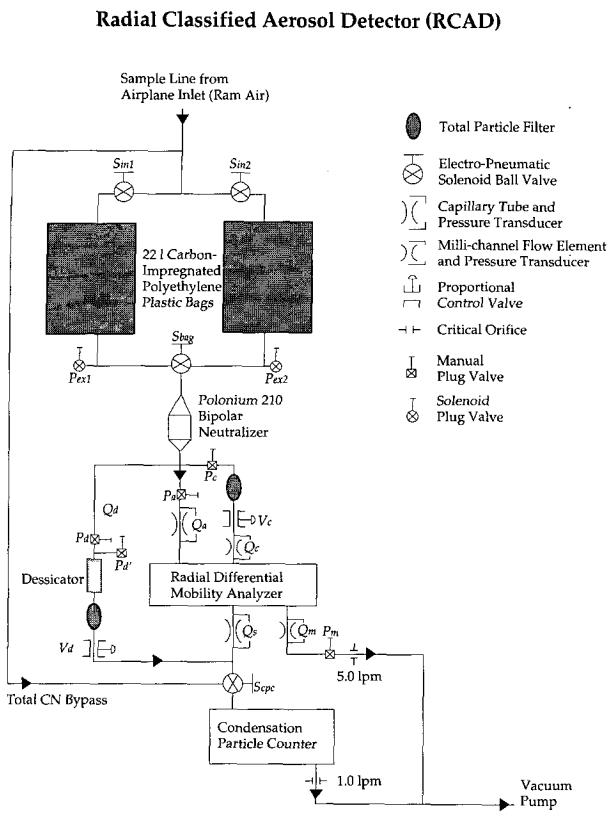

FIG. 1. Components and configuration of the radially classified aerosol detector (RCAD).

changes. Mobility classification requires precise control of several coupled flow rates. Continuous measurements require immediate and accurate adjustment of those flows in response to changes caused by pressure variations.

3. Instrument design

A radially classified aerosol detector (RCAD) has been developed for unattended, high-resolution airborne measurement of particle size distributions of atmospheric aerosols. The principal components of the system are an alternating grab-bag sampler, an aerosol charger-neutralizer, a radial differential mobility analyzer (RDMA), and an ultrafine condensation particle counter (CPC). The integrated size measurement system is shown schematically in Fig. 1. Through a series of valves, the bag sampler captures a fixed volume of air from which the aerosol is drawn into the classifier and detector. After filling a bag, flow is extracted at approximately 6 L min^{-1} through the radioactive charger in which the aerosol attains a steady-state bipolar charge distribution.

The RDMA effectively eliminates most of the signal degradation associated with diffusion broadening in conventional electrostatic classifiers (Zhang et al. 1995). The RDMA has an aerosol inlet with minimal particle losses and a residence time one-fifth that of the most common commercial cylindrical DMA (TSI, model 3071), leading to reduced diffusion losses and broadening for small particles. In addition, as shown in Table 2, the RDMA is more compact and lighter weight than its cylindrical counterparts, thus facilitating its use aboard aircraft. We have further enhanced this instrument by extending the range of sizes that can be measured by employing an analog voltage ramp circuit to control the high voltage applied across the classifier, thereby providing accurate voltage control over four decades.

The ultrafine CPC combines the condensation efficiency of ultrafine particles in the Stolzenburg and McMurry (1989) design with the higher flow rates of conventional clean-room type CPCs. As a result, counting rates are sufficiently large to provide adequate signal-to-noise ratios even at low number concentrations. Counting efficiency for ultrafine particles was improved by increasing the difference in temperatures in the saturator and the condenser. The resulting instrument shows both high efficiency in detecting ultrafine particles and good counting statistics at low concentrations.

TABLE 2. Dimensions of six differential mobility analyzer (DMA) designs.

Geometry	Group	Reference	Diameter range[a]	Dimensions[b] ($H \times D$)
Cylindrical—"long"	TSI, Inc.	Knutson and Whitby (1975)	0.020–1.000 μm	44 cm × 3.9 cm
	NRL	Hoppel (1978)	0.010–1.2 μm	86 cm × 10 cm
	Hauke	Winklmayr et al. (1991)	0.010–1.000 μm	60 cm × 6.6 cm
Cylindrical—"short"	TSI, Inc.	Adachi et al. (1990)	0.002–0.001 μm	10 cm × 3.9 cm
	Hauke	Winklmayr et al. (1991)	0.001[c]–0.150 μm	11 cm × 6.6 cm
Radial	ISPN	Fissan et al. (1994)	0.007–1.000 μm	0.4 cm × 13 cm
	CIT	Zhang et al. (1995)	0.003[d]–0.500 μm	1.0 cm × 10 cm

[a] Unless otherwise noted, the lower bound is the 50% cutoff in transmission efficiency.
[b] Dimensions given are outer dimensions of flow volume. In each case the height (H) and diameter (D) are given.
[c] Transmission efficiencies were not measured. Lower bound is range specified in paper.
[d] Transmission efficiency measured at this diameter is 92%. No data are available for smaller sizes.

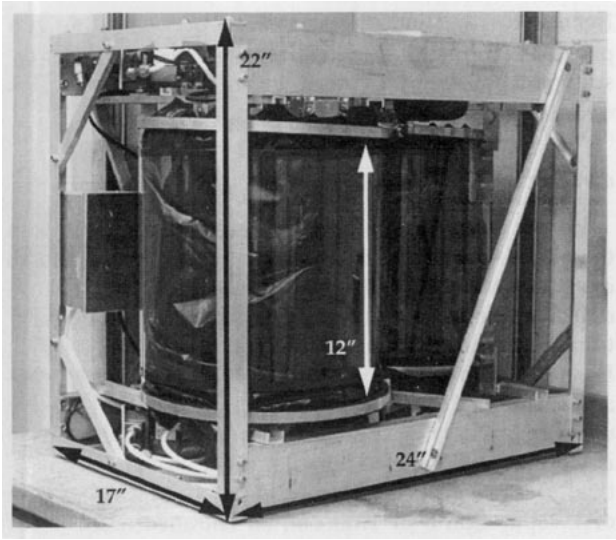

FIG. 2. Grab sampling apparatus. The aluminum frame is designed to mount in a standard 19″ rack. The apparatus weighs 35 kg.

a. Alternating double-bag sampler

The grab-bag sampling system operates with two identical sampling bags in parallel, such that one bag may be flushed then filled while the other bag is used for measuring the collected aerosol. The photograph in Fig. 2 shows the dimensions of the apparatus. The valves regulating the direction of aerosol flow employ ball valves operated by an electropneumatic solenoid system (Whitey). The bags are constructed from custom-cut carbon-impregnated polyethylene mounted between two steel-shim-covered Plexiglas disks. The air enters the aircraft through 1.9-cm (i.d.) tubing (carbon-impregnated polyethylene), shown in Fig. 1.

b. Neutralizer

A bipolar neutralizer containing four Polonium 210 static strips (Static Master, model 2U500) was employed to charge the aerosol sample. The charger casing was designed to maximize uniform exposure to the polonium alpha emissions while minimizing dead time and mixing and is illustrated in Fig. 3. The 7° angle at the neutralizer entrance prevents recirculation of streamlines. The neutralizer was designed to attain an equilibrium charge distribution for residence times corresponding to flow rates of up to 15 L min^{-1} but has been operated at 6 L min^{-1}. The charge distribution resulting by diffusion charging of particles by collision with ions produced by alpha particles is described by Wiedensohler (1988) in Fig. 4. The charging probability has been checked experimentally (D. Covert 1995, personal communication) and was found to be within the experimental uncertainty of the theoretically expected value for distributing an equilibrium charge on a charged aerosol.

Static-Strip Bipolar Neutralizer

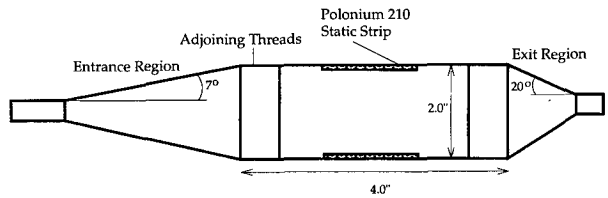

FIG. 3. Design of the housing for a bipolar charger that supports four polonium 210 static strips, modified from earlier work at Aerosol Dynamics, Inc.

c. Flow control

The flow passing through the neutralizer is divided into three streams as illustrated in Fig. 1: the aerosol and clean sheath flows for the RDMA (Q_a and Q_c, respectively) and the dilution flow to the CPC (Q_d). The electric field controlled by the voltage difference between the two parallel disks in the RDMA selects particles of a narrow range of mobilities into the sample flow (Q_s) exiting the RDMA, while the main excess flow (Q_m) removes the remainder of the flow. The sample flow is mixed with the dilution flow, which has been filtered and dried. The three-way valve (S_{cpc}) at the

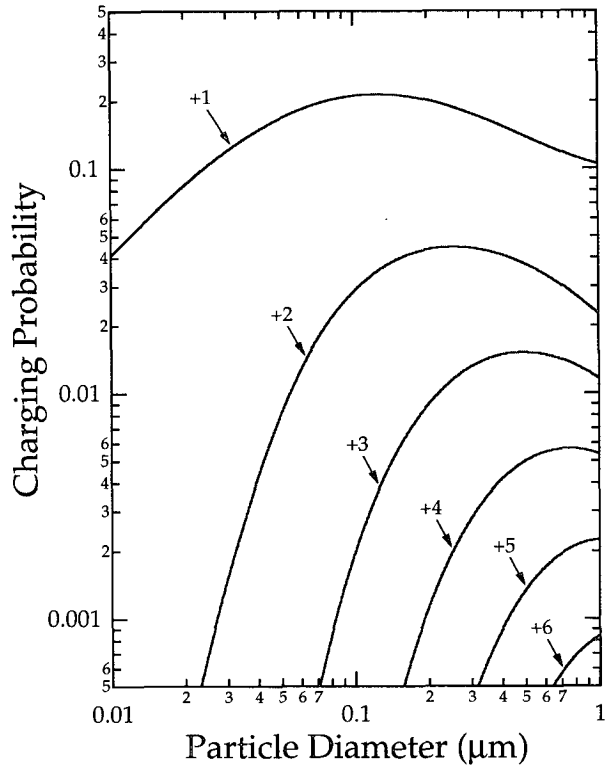

FIG. 4. Particle charging efficiency in the bipolar neutralizer based on calculations described in Fuchs (1963) and Wiedensohler (1988).

CPC inlet allows direct sampling of the inlet stream by bypassing the bag sampler and RDMA. The CPC flow is set by a 1 L min^{-1} critical orifice. The excess RDMA flow (Q_m) exits the main outlet of the RDMA to a 5 L min^{-1} critical orifice. At the Q_m stream exiting the RDMA, probes are installed to monitor temperature and relative humidity (Vaisala, Woburn, Massachusetts), and pressure is measured with an absolute pressure transducer (Validyne, Northridge, California). The flows controlled by the two critical orifices are pulled by a vacuum pump connected downstream.

Four flow rates are monitored in the system by measuring the pressure drop with electronic differential pressure transducers (Validyne) across laminar flow elements in the lines. In the sheath flow lines (Q_c and Q_m) of 5 L min^{-1}, the pressure drops consist of "millichannel flow elements," consisting of more than 100-mm-width parallel channels formed by corrugated stainless steel shim stock with pressure taps just upstream and downstream of the restriction. In the aerosol flow lines (Q_a and Q_s) of 0.5 L min^{-1}, each restriction consists of a capillary tube with one pressure tap far enough downstream from the entrance to be beyond the hydrodynamic development region of the flow and a second pressure tap just before the capillary exit. The relationship of pressure drop to flow through the restrictions is linear for the flow ranges for both elements. The transducer output signals are proportional to the pressure drops. Five plug valves (P_c, P_m, P_a, P_d, $P_{d'}$) in the system along with the valve S_{cpc} allow isolation of the aerosol and sheath flows so that the flow transducers can be calibrated in place with a flowmeter standard installed upstream of the charger.

Five flows—Q_a, Q_c, Q_s, Q_m, and Q_d—are fixed by three steady-state relationships and two controlled ratios in the RCAD system. Two of the relationships are set by critical orifices:

$$Q_m = 5.0 \text{ L min}^{-1} \quad (1)$$

$$Q_s + Q_d = 1.0 \text{ L min}^{-1}, \quad (2)$$

and the steady-state mass balance for the four RDMA flows provides an additional condition:

$$Q_a + Q_c = Q_s + Q_m. \quad (3)$$

Continuous monitoring of the four flows allows the flow control system to respond to variations in the sampling pressure. Deviations from the setpoint in the four RDMA flows are used to control two independent controllers: one maintains a constant RDMA inlet flow ratio and the other a constant RDMA outlet flow ratio:

$$\frac{Q_a}{Q_c} = 0.1 \quad (4)$$

$$\frac{Q_s}{Q_m} = 0.1. \quad (5)$$

Because of the linear relationships between flow and pressure drop across the restrictions, this algorithm results in a constant flow ratio within a few tenths of 1% over the limited range of operation.

d. Radial DMA

Zhang et al. (1995) have characterized the losses in the RDMA, and their data have been interpolated to estimate the losses at the flow rates used here. The radial DMA operates in a manner similar to a conventional cylindrical DMA (Knutson and Whitby 1975; Hoppel 1978) but is designed to reduce residence times and diffusion losses so that it can effectively measure ultrafine particles as small as 3 nm. The RDMA used in the system described here has inner dimensions identical to those described by Zhang et al. (1995), with a disk separation h of 1.00 cm, an entrance radius r_2 of 5.09 cm, and an exit radius r_1 of 0.25 cm, but it has been modified to minimize its weight by thinning the outer dimensions and using Delrin© in place of steel for structural support. The resulting classifier weighs 4 kg and is 5 cm thick and 20 cm in diameter. It is fastened to vertical struts and rests on a notched and rubber-lined aluminum support. The absolute pressure is monitored in the RDMA with a transducer (Validyne) mounted at the excess flow exit (Q_m), and relative humidity and temperature are measured with probes downstream.

e. Voltage ramp

Rapid mobility measurements are made by classifying particles in an electric field that varies exponentially with time (Wang and Flagan 1990). In both the original implementations of this method and its recent commercial version (TSI scanning mobility particle sizer), the high voltage was controlled using a high-resolution (16 bit) digital-to-analog converter. Although this approach produces a smooth exponential ramp at high voltages, the discrete voltage steps become appreciable at low voltages, introducing uncertainty at the fine-particle end of the size spectrum.

In the RCAD, a smooth exponential ramp is provided over the entire voltage range using an analog exponential ramp circuit (ERC) that consists of an integrator and an inverter–follower. This circuit, illustrated in Fig. 5, provides a 0–5-V analog signal that drives the high voltage module (Bertan, model 602C-100N:CS2562) to provide voltage output of 3–10 000 V. For an increasing voltage ramp, the second operational amplifier functions as an inverter, while it serves as a follower to provide a decreasing voltage ramp. The characteristic time for the voltage ramp τ_r, defined by the relation

$$V = V_0 \exp\left(\pm \frac{t}{\tau_r}\right), \quad (6)$$

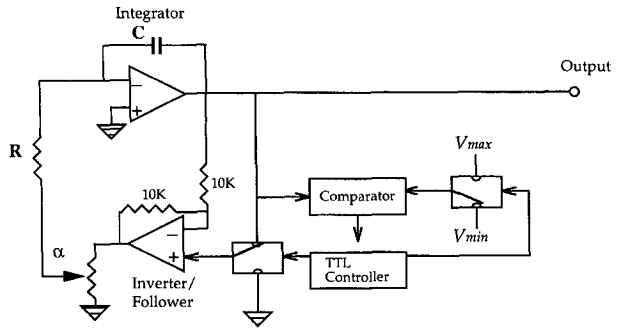

FIG. 5. Exponential ramp circuit (ERC).

where

$$V_0 = \begin{cases} V_{\min}, & \text{for increasing scan or ``upscan,'' denoted SEMSu} \\ V_{\max}, & \text{for decreasing scans or ``downscan,'' denoted SEMSd,} \end{cases}$$

is determined in the ERC circuit by

$$\tau_r \equiv \frac{RC}{\alpha}, \tag{7}$$

where α is the potentiometer ratio in the circuit and provides coarse adjustment of τ_r. The capacitance C is fixed. The voltage ramp τ_r is varied by changing R, with fine adjustment being provided with a 10-turn potentiometer. The ERC ramp is initiated by a TTL (transistor transistor logic) low pulse. When the ramping voltage reaches $V_{\min}$ or $V_{\max}$, the comparator sends a signal to the TTL circuit, thus changing the analog switch to convert the operational amplifier from an inverter to a follower.

f. Turbo CPC

Condensation particle counters operate on the principle of growing aerosol particles from the fine or ultrafine size range to sizes that are large enough to be optically detected. The sample is first saturated with condensible vapor at an elevated temperature (T_s) in the saturator; the vapor is then condensed onto the particles by cooling the sample stream to T_c in the condenser. The supersaturation in the condenser, and hence the probability that particles of a given size will grow by condensation, is controlled primarily by the difference in the temperatures T_s and T_c, as described by the following relation based on the Clausius–Clapeyron equation for liquid-gas equilibrium:

$$S \equiv \frac{P_c}{P_{\text{sat}}(T_c)} = \frac{P_{\text{sat}}(T_s)}{P_{\text{sat}}(T_c)} = \exp\left[\frac{\Delta H_v}{R}\left(\frac{1}{T_c} - \frac{1}{T_s}\right)\right], \tag{8}$$

where ΔH_v is the vapor's latent heat of vaporization.

Scanning mobility measurements limit the time available for counting particles in any channel. Acquiring a statistically significant number of counts within the available counting time (1 s) requires that particles be counted from a large sample flow rate. The TSI model 3010 condensation particle counter provides an adequate flow rate (1 L min^{-1}), but its 50% detection cutoff is 12 nm in its standard configuration (Quant et al. 1992). In order to extend its detection limit to smaller sizes, a modified instrument was constructed that increased the temperature difference $\Delta T = T_s - T_c$ from the nominal value of 17°C. Laboratory results had previously shown that this cutoff could be decreased to 8 nm by increasing ΔT to 25°C. By augmenting the heating capabilities in the saturator with a heating mat and the cooling in the condenser with an additional thermoelectric device (TED) placed adjacent to the original TED, the counting efficiency can be further enhanced. These modifications were implemented in a custom-built 3010 CPC (TSI) that has been dubbed the "Turbo 3010." In the original 3010 CPC, only the temperature difference ΔT is controlled. Specifying only ΔT can lead to drift in T_s and T_c as the operating conditions (e.g., cabin temperature) shift. Since the supersaturation in the condenser is sensitive to the absolute temperature, this drift can alter the expected counting efficiency of the instrument. The EPROM (erasable programmable read-only memory) chip in the CPC was modified to allow T_s and T_c to be specified and controlled independently to 38° and 2°C, respectively, eliminating the sensitivity of the instrument performance to the ambient (cabin) temperature. The counting efficiency was measured by comparison of calibration aerosols of salt and agglomerated silver with an electrometer standard for particles as small as 4.5 nm.

g. RCAD software

Software to drive each of these components synchronously and to record data from them was written using a C-compatible development program (National Instruments, LabWindows CVI) on a notebook-style computer (IBM, Thinkpad 750). The user interface allows the user to initiate different modes of operation (automatic or manual trigger) and switch sampling ports (bag sampling or DMA bypass), while monitoring the flow rates, temperature, pressure, humidity, valve states, and CPC performance. Digital and analog data acquisition are accomplished with a PCMCIA card with 16 single-ended analog channels and 16 digital input–output channels (National Instruments, DAQCard 700). The software coordinates the filling and sampling from the double-bag sampler so that a sample is drawn immediately after a bag is filled. The voltage ramp in the RDMA is started after a 5-s delay to allow new sample to reach the DMA and the flow controls to reestablish constant flow ratios after the perturbation of the valve switch. Particle counts detected by the CPC

during 1-s intervals are transmitted serially from the CPC to the computer using the hardware-coded EPROM downloading commands in the CPC. A real-time display shows the raw counts recorded against the current RDMA voltage, so that the raw data illustrate general distribution characteristics on a time-shifted axis.

4. Characterization of instrument components

The performance of each of the instrument components described above has been characterized. Losses in aerosol transport lines have been estimated theoretically. The RDMA and CPC have been calibrated to determine the particle transmission efficiency and instrument response functions. This section summarizes these instrument characterization studies.

a. Particle losses in tubing and sampling chamber

An essential part of an aerosol sampling system is the design of the plumbing so as to minimize particle losses in the sampling train. These losses may be estimated with careful calculations. Particle losses may also occur in the RDMA. Particle losses expected in the tubing preceding the detector can be estimated from the expected diffusion of particles in known flow conditions.

The flow rate in the 1.9-cm tubing preceding the sampling chamber is driven by ram pressure, which for a typical aircraft speed of 100 m s^{-1} is estimated to be 470 L min^{-1}. This flow has a Reynolds number of 38 000 for air of density 1.2 kg m^{-3} and viscosity 2.0 kg m^{-3} s^{-1}. If we define ϕ to be the number concentration of particles remaining at the end of tubing of length L and diameter d for an entrance number concentration of ϕ_0 particles and flow rate Q, then for turbulent flow conditions, the particle losses may be determined from

$$\frac{\phi}{\phi_0} = \exp\left(-\frac{\pi d L k}{Q}\right), \tag{9}$$

where the mass transfer coefficient k is given by (Friedlander 1977)

$$\frac{kd}{D} = 0.079\ \mathrm{Re} f^{1/2}\ \mathrm{Sc}^{1/4}, \tag{10}$$

where Re is the Reynolds number, Sc the Schmidt number, f the friction factor for the flow conditions, and D is the diffusivity of the particles.

The air sample is held in the chamber for less than 1 min. Figure 6 illustrates the bounds on the particle losses in the chamber calculated based on the eddy diffusivity for the range of flow rates at which air is withdrawn from the sampler. The turbulent kinetic energy introduced in the sampling chamber by the fill rate of the inlet of about 500 L min^{-1} decays rapidly, such that

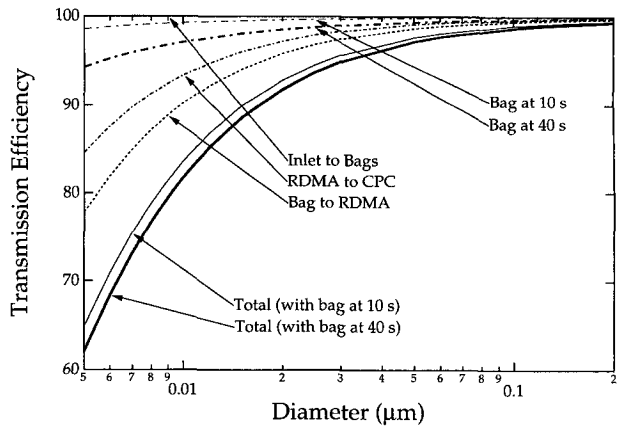

FIG. 6. Particle transmission efficiency through the inlet tubing, the bag sampler, the connections from the bag sampler to the RDMA, and from the RDMA to the CPC. The transmission efficiency for each section is described as the concentration of particles persisting, ϕ, divided by the inlet concentration of particles, ϕ_0. The broken lines illustrate contributions from each of the segments described, as well as for the losses in the bag for holding times of 10 s (thin alternating dashes) and 40 s (thick alternating dashes). The solid lines show the total losses expected for all of the instrument regions for bag holding times of both 10 s (thin broken line) and 40 s (thick broken line).

the eddy diffusivity for the sample holding period can be estimated from eddies generated by the withdrawal of air from the chamber using the expression proposed by Okuyama et al. (1977):

$$k_e = 0.00918 Q^{3/2}. \tag{11}$$

The losses can then be calculated from the particle deposition coefficient, β, where

$$\beta = \frac{v}{H} + \frac{SD}{\Upsilon\sigma} \tag{12}$$

for particles of settling velocity v and a vessel of height H, surface area S, volume Υ, and a diffusion boundary layer σ, which may be calculated from k_e (Crump and Seinfeld 1981). Then

$$\frac{\phi}{\phi_0} = \exp(-\beta t). \tag{13}$$

The bag volume shrinks continuously during sampling, beginning at a volume of 22 L and ending at a volume of 16 L; the calculation is done by integrating over the sampling period.

The air withdrawn out of the chamber flows at 6 L min^{-1} and is then split so that 0.5 L min^{-1} of sample air transits the DMA before it is diluted to 1 L min^{-1} and enters the detector. An upper bound on the straight tube losses for these regimes of laminar flow may be estimated from the expression provided by Gormley and Kennedy (1949) for laminar flow:

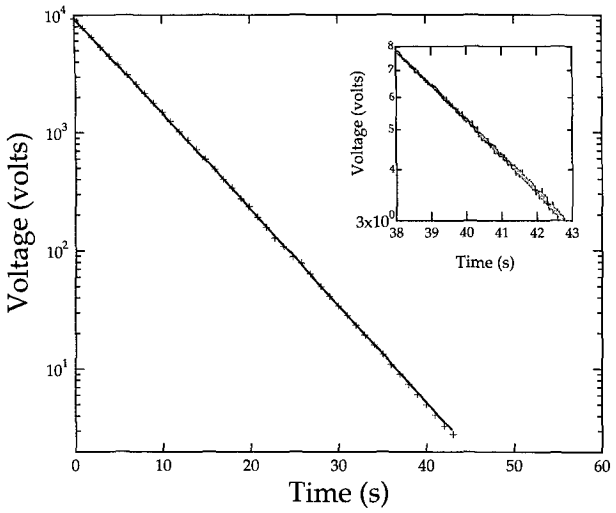

FIG. 7. Performance of the exponential ramp circuit is illustrated by a plot of increasing and decreasing voltage with time. Data points illustrate voltages (on a logarithmic scale) measured at 1-s intervals, and the solid lines show the exponential ideal function of the form indicated by Eqs. (6) and (7), with τ_r = 5.35 s, V_{low} = 3 V and V_{high} = 9490 V. The inset illustrates high-resolution data (100 Hz) for the lowest voltages on an expanded log scale.

$$\frac{\phi}{\phi_0} = 1 - 2.56\eta^{2/3} + 1.2\eta + 0.177\eta^{4/3}, \quad \eta \leq 0.01, \tag{14}$$

where

$$\eta = \frac{\pi DL}{Q}. \tag{15}$$

Figure 6 illustrates the combined magnitude of each of these particle losses. These losses occur sequentially and are proportional to the particle number concentration, so that the overall losses are the product of each of these contributions and are also illustrated in Fig. 6. Since particle diffusion losses are dependent on Brownian diffusivity, ultrafine particles will be most affected; 35% of 5-nm particles are estimated to be lost by diffusion in the tubing and bag sampler (for a 10-s holding time) as illustrated in Fig. 6, whereas less than 1% of 200-nm particles are lost.

b. *Classifier resolution*

Resolution of the particle classification possible with the RDMA is presented in Zhang et al. (1995). Expected diffusion losses for ultrafine particles are significantly lower than for conventional cylindrical DMAs (Knutson and Whitby 1975; Hoppel 1978; Winklmayr et al. 1991). For the flow rates used here, the diffusion loss data from Zhang et al. (1995) may be interpolated to provide the estimate of expected diffusion losses of particles in the RDMA at the flow rates used for this configuration. The transfer function for the RDMA has the same functional form as that for the cylindrical DMA, although the geometric factors differ for the two instruments. The selection of particle size is controlled by the voltage applied to the RDMA, which is controlled by the ERC. The operation of the ERC is compared to the exponential rate predicted theoretically from Eq. (3) in Fig. 7.

c. *Particle counting efficiency*

The counting efficiency of the modified particle counter was determined by comparing the modified counter's performance to a known electrometer standard (TSI, model 3068A). The apparatus for this calibration study is illustrated in Fig. 8. A vaporization–condensation source generated aerosol at a flow of 2 L min^{-1} (Scheibel and Porstendörfer 1983) that was classified to a known particle size in a mobility classifier (TSI, model 3071) and then diluted to 22 L min^{-1}

Particle Counter Calibration Apparatus

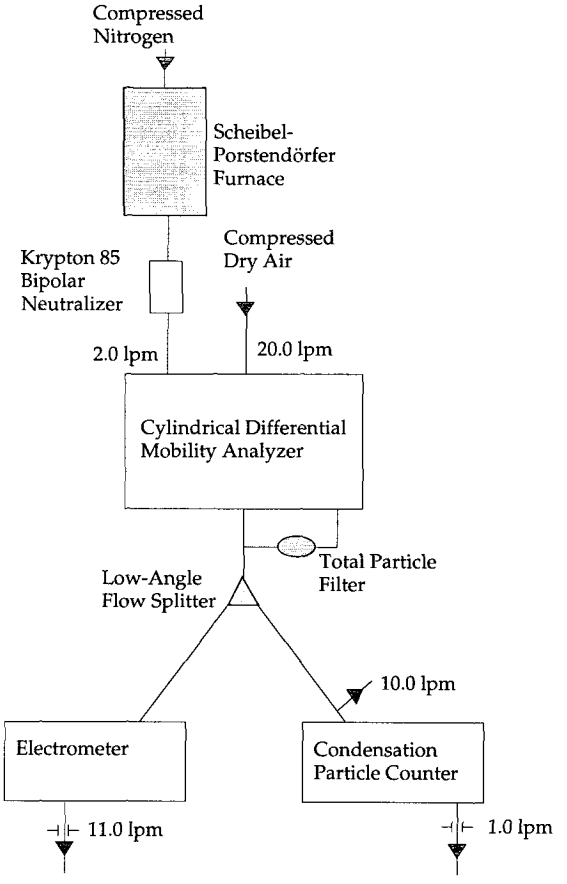

FIG. 8. Apparatus for calibration of modified condensation particle counter.

with particle-free air. The resulting flow was divided equally in a low-angle flow splitter (TSI, model 2009) between the electrometer (calibrated at 11 L min^{-1}) and the modified CPC (pulling 1 L min^{-1} with 10 L min^{-1} bypass flow). The tubing leading to both instruments was identical up to the instrument entrances, using flexible conductive tubing to connect the flow splitter to the inlets. Hence, the number of particles counted in both cases could be compared in order to calculate the counting efficiencies. The results of these experiments are illustrated in Fig. 9 for two types of source aerosol, silver (Ag), and salt (NaCl).

A potential limitation in improving counting efficiency by increasing ΔT is the possible artifact of homogeneous nucleation in the CPC leading to spurious counts in the measurements. The conditions most susceptible to allowing homogeneous nucleation are high supersaturation of condensible vapor and low preexisting aerosol surface area (Seinfeld 1986). For ΔT up to 36°C, no particles were detected for a particle-free airstream, demonstrating that for the operating temperatures of T_s = 38°C and T_c = 2°C spurious counts should not be detected.

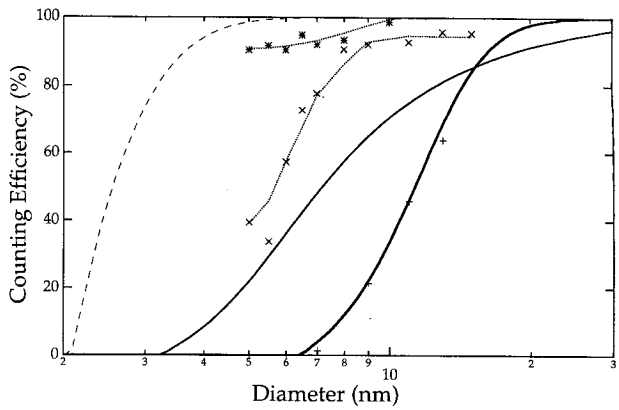

FIG. 9. Particle counting efficiency for the modified CPC, compared with several commercially available models. The data were taken with the apparatus illustrated in Fig. 8, where salt (NaCl) was used to generate aerosol for the ΔT = 25°C data, indicated by crosses (×), and silver (Ag) for the ΔT = 17°C and ΔT = 36°C data, indicated by pluses (+) and asterisks (*), respectively. The thick solid, thin solid, and broken lines indicate the calibration curve of a standard TSI 3010 CPC, 3022 CPC, and 3025 CPC, respectively (Quant et al. 1992).

d. Kernel function for RCAD operation

The measurement capabilities of the instrument are described by the probability that a particle of a given size will be detected, and this relationship is known as the instrument's kernel function. The kernel function for the RCAD is defined by the following relationship for the counts recorded in the ith measurement channel

$$S_i = \int_0^\infty k_i(D_p) f(D_p) dD_p + \epsilon_i \quad i = 1, 2, \cdots, n, \quad (16)$$

where $f(D_p)$ is the particle size distribution that is defined such that $f(D_p)dD_p$ is the number concentration of particles with diameters between D_p and $D_p + dD_p$, $k_i(D_p)$ is the so-called kernel function for channel i, n is the total number of measurement channels, and ϵ_i is the noise that is inherent in any experimental measurement (Russell et al. 1995). Detailed knowledge of the kernel function is a prerequisite for determination of the particle size distribution from the recorded signals. Russell et al. (1995) define the kernel function for DMA measurements of the particle size distribution in terms of experimental parameters as

$$k_i(D_p) = Q_a \sum_\nu s(D_p, \nu) \phi_\nu(D_p) \bar{\Omega}_i[\zeta(\nu, D_p)], \quad (17)$$

where $s(D_p, \nu)$ is the probability that the detector will count a particle of diameter D_p with ν charges, $\phi_\nu(D_p)$ is the fraction of particles of diameter D_p carrying an elementary charge of ν, Q_a is the volumetric flow rate of aerosol entering the DMA, and $\bar{\Omega}_i[\zeta(\nu, D_p)]$ is the fraction of the particles of dimensionless mobility $\zeta(\nu, D_p)$ that will exit the analyzer during the counting interval of channel i. Note that the measurement procedure used here used sufficiently long delays between scans so that carryover effects from previous scans can be neglected; hence, we have omitted references to the scan number in the subscripts of the kernel (k) and transfer (Ω) functions. For the RDMA,

$$\zeta(\nu, D_p) = \frac{2\pi V_0}{Q_s + Q_a} \frac{r_2^2 - r_1^2}{h} \frac{\nu e C_c}{3\pi\mu D_p}, \quad (18)$$

where C_c is the Cunningham correction factor, e is the charge of an electron, and μ is the viscosity of the carrier gas (Zhang et al. 1995). For exponential voltage scanning operation, $\bar{\Omega}_i[\zeta(\nu, D_p)]$ is replaced by $\bar{\Omega}_i^e[\zeta(\nu, D_p)]$, which can be shown to be dependent on the flow characteristics of the instrument configuration (Russell et al. 1995). The characteristic mixing time for the instrument (τ_s) and the corresponding plumbing time (τ_p) have been evaluated for the RCAD's intrainstrument plumbing. The response of the CPC to a step change in concentration at the classifier was measured by recording particle counts as a function of time as the voltage at the classifier is switched from 500 to 0 V, with the resulting concentrations plotted in Fig. 10. The best fit to the resulting residence time distribution was obtained for τ_p = 8.0 s and τ_s = 1.1 s, corresponding to the modeled flow pattern illustrated in Fig. 10 by the solid line.

A significant advance in the speed of operation of the differential mobility analyzer can be achieved when the voltage is scanned continuously rather than stepped in increments (Wang and Flagan 1990). The operation of a DMA in scanning-mode operation at a given measurement speed differs from stepping-mode operation

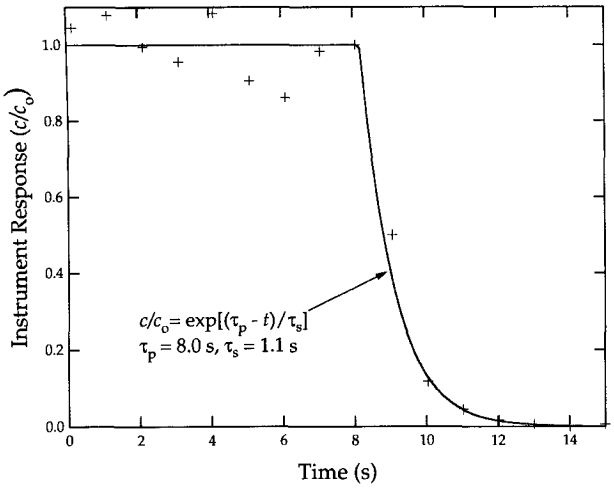

FIG. 10. Response of the RCAD to a step change in concentration at the classifier. The line illustrates the flow model used to represent the residence time distribution.

in that the characteristic mixing time of the DMA-CPC configuration limits the speed with which the voltage can be scanned (Russell et al. 1995). This limitation of the scanning speed is, in fact, independent of the geometry of the DMA (i.e., radial versus cylindrical), as it results entirely from the residence time of particles from the exit of the DMA to the point of detection in the CPC (which are determined by the plumbing configuration and the CPC geometry). The dependence of scan accuracy on the flow configuration between the instruments has been investigated experimentally by Flagan et al. (1993), showing that fast measurement speeds result in the asymmetric response described by Russell et al. (1995).

This flow pattern is then used to calculate the kernel function for each instrument channel, as illustrated by the representative channels shown in Fig. 11. Estimation of the particle size distribution requires solution of the set of Fredholm integral equations [Eq. (16)] for the n experimental measurements. For this purpose, the MICRON algorithm is employed to retrieve size distributions from each set of scanned measurements (Wolfenbarger and Seinfeld 1990).

5. In-flight performance

The RCAD instrument package described above has been mounted aboard the University of Washington C131a research aircraft. A series of flights based out of Monterey, California, during June 1994, provided an opportunity to demonstrate the performance of the instrument in measurement of aerosol size distributions in the marine boundary layer. For this purpose, the measurement conditions in the instrument were carefully monitored. Results are presented here for in-flight variations in temperature, relative humidity, pressure, and flow. Temperature and pressures monitored in the airstream are used to correct the kernel function in order to interpret the data signals since particle mobility is a function of both air pressure and temperature.

a. Temperature and humidity

The air sample entering the instrument is heated from the ambient temperature by deceleration of the air on entering the aircraft. The resulting temperature is plotted in Fig. 12. The instrument and cabin temperature measurements have electrically generated noise in the signals resulting in ±3°C. In Fig. 12, these fluctuations have been removed by evaluating the mean values for each 45-s measurement period. The temperature of the air at the point of measurement in the classifier tracks the cabin temperature closely since heating of the instrument package can result in additional warming of the sampled air.

During the course of the flight, an increase in the aircraft cabin temperature can preclude the CPC condenser from maintaining the temperature setpoint of 2°C. The resulting drift in the temperatures of the saturator and the condenser will alter the counting efficiency for ultrafine particles. By monitoring the temperatures of the saturator and condenser as illustrated in Fig. 12, we can correct for diminished CPC performance for each size distribution.

Heating of the sampled air dries the airstream so that the humidity at which particles are measured is between

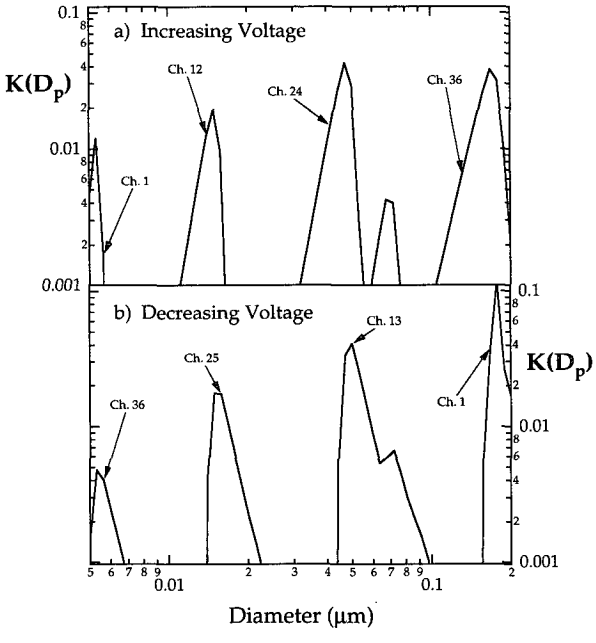

FIG. 11. Kernel function of (a) an increasing-voltage scan of the RCAD system and (b) a decreasing-voltage scan of the RCAD system. Channels 1, 12, 24, and 36 are illustrated for an increasing voltage scan, and the corresponding channels (channels 1, 13, 25, and 36) are illustrated for a decreasing voltage scan.

20% and 40% throughout the flight. The resulting particle sizes measured are dry nuclei diameters.

b. Pressure and flow rates

Air is drawn into the instrument from the bag sampler, which is in equilibrium with the aircraft's unpressurized cabin. Consequently, the pressure in the instrument varies with altitude. The feedback algorithm used in controlling the flow rates in the instrument provides constant volumetric flow rates in the instrument, so that the shape of the transfer function, and hence the size resolution of the measurement, is maintained. The effectiveness of the control algorithm is illustrated by Fig. 13 in which the flow rates are illustrated for a single flight, during both ascents and descents through the boundary layer. The high-frequency fluctuations of ±6 torr in pressure result in part from electrically generated noise in the signal.

When the absolute pressure within the system changes due to ascent or descent of the aircraft, flow imbalances develop within the system. In particular, conservation of mass dictates a net inflow to or outflow from the RDMA in order to effect a change in the pressure of the finite volume of air contained therein. During such changes the controllers still maintain constant inlet and outlet flow ratios, thereby maintaining the shape of the RDMA transfer function under these transient conditions.

In Fig. 13, the switch between the dual sampling bags is marked by a spike in the flow rates of ±0.5 L min^{-1} in Q_c and ±0.3 L min^{-1} in Q_a. Switching between bags results in an interruption of the flow to the instrument, which must be compensated by the flow control. These perturbations are almost instantaneous, corresponding to the valve actuation time of much less than 1 s. From the 1-Hz frequency data illustrated in Fig. 13, the recovery time of the flow rates is estimated to be less than 1 s, so that the flow has stabilized before data is recorded for the measurement. Electrical noise in the flow metering results in around ±1% of the reported flow rates.

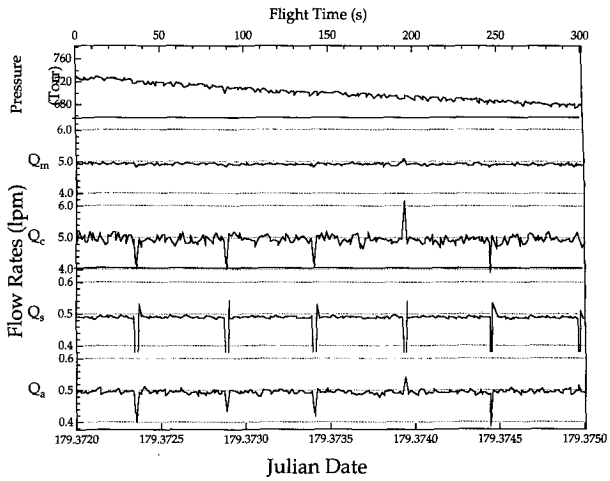

FIG. 13. Performance of the flow control system in flight on 28 June 1994, during an ascent through the boundary layer that resulted in a pressure drop of 50 torr in 300 s.

Changes in pressure corresponding to altitude changes of the aircraft occur at gradual rates corresponding to the climb or descent rate of the aircraft. For the time period illustrated in Fig. 13, the pressure drops 50 torr during 300 s. Adjusting the flow rate to the resulting gradual change in absolute pressure in the instrument requires fine adjustment of the flows. As shown in Fig. 13, the volumetric flow rates are maintained to their designed flow settings during sampling intervals within the precision of the flow measurement for the time period illustrated.

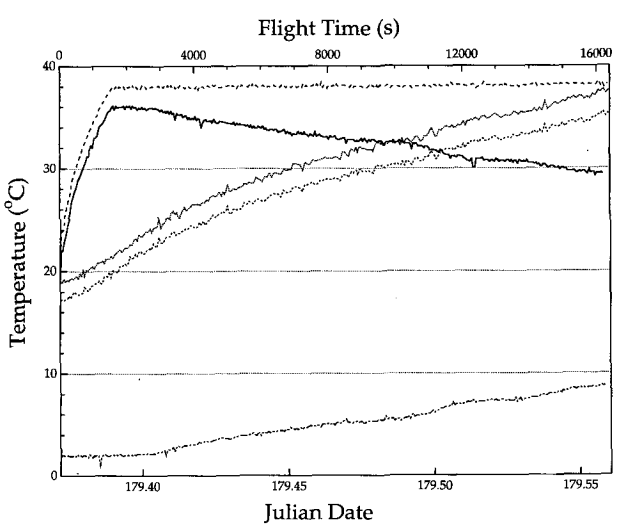

FIG. 12. Illustration of temperature variation in flight. The temperature in the CPC condenser (T_c, indicated by the alternating dashed line) and saturator (T_s, indicated by the long-dashed line) varies with changes in cabin temperature (shown as a dotted line) and instrument temperature (short-dashed line) during a flight on the University of Washington C131a aircraft on 28 June 1994. The temperature difference, $\Delta T = T_s - T_c$, is also illustrated by the solid line.

Acknowledgments. The authors are grateful for the help of the University of Washington Cloud and Aerosol research group for their assistance in integrating the RCAD into the C131a, with special thanks to Dean Hegg, Ron Ferek, Peter Hobbs, Jack Russell, and Don Spurgeon. The use of the laboratories of TSI, Inc., and the support of Fred Quant, Rick Holm, Maynard Havlicek, and Gil Sem were indispensable in constructing and calibrating the modified CPC. The financial support of the Office of Naval Research Grants N00014-93-1-0872 and N00014-94-1-0663 is gratefully acknowledged, both for development of the RCAD and the flights scheduled as part of the Monterey Area Ship Track (MAST) Experiment.

REFERENCES

Adachi, M., K. Okuyama, Y. Kousaka, S. W. Moon, and J. H. Seinfeld, 1990: Facilitated aerosol sizing using the differential mobility analyzer. *Aerosol Sci. Technol.*, **12,** 225–239.

Brock, C. A., L. F. Radke, J. H. Lyons, and P. V. Hobbs, 1989: Arctic hazes in summer over Greenland and the North American Arctic I: Incidence and origins. *J. Atmos. Chem.*, **9,** 129–148.

Clarke, A. D., 1991: A thermo-optic technique for in-situ analysis of size-resolved aerosol physicochemistry. *Atmos. Environ.*, **25A,** 635–644.

——, 1993: Airborne measurements of aerosol properties in clean and polluted air masses during ASTEX. *Proc. 1993 AGU Spring Meeting,* Baltimore, MD, American Geophysical Union.

Conover, J. H., 1966: Anomalous cloud lines. *J. Atmos. Sci.,* **23,** 778–785.

Crump, J. G., and J. H. Seinfeld, 1981: Turbulent deposition and gravitational sedimentation of an aerosol in a vessel of arbitrary shape. *J. Aerosol Sci.,* **12,** 405–415.

——, R. C. Flagan, and J. H. Seinfeld, 1983: Particle wall loss rates in vessels. *Aerosol Sci. Technol.,* **2,** pp. 303.

Daum, P. H., and S. R. Springston, 1993: Tropospheric sampling with aircraft. *Measurement Challenges in Atmospheric Chemistry,* American Chemical Society, 101–132.

Fissan, H., P. Büscher, S. Neumann, F. Stratmann, D.-R. Chen, and D. Y. H. Pui, 1994: Experimental comparison of four differential mobility analyzers for nanometer aerosol measurements. *Fourth Int. Aerosol Research Conf.,* Los Angeles, CA, American Association for Atmospheric Research, pp. 462.

Flagan, R. C., F. R. Quant, K. D. Horton, L. M. Russell, G. J. Sem, and M. M. Havlicek, 1993: Scanning mobility particle sizer characterization and intercomparison. *12th Amer. Assoc. Aerosol Research Conf.,* Oak Brook, IL, American Association for Atmospheric Research, p. 292.

Frick, G. M., and W. A. Hoppel, 1993: Airship measurements of aerosol size distributions, cloud droplet spectra, and trace gas concentrations in the marine boundary layer. *Bull. Amer. Meteor. Soc.,* **74,** 2195–2202.

Friedlander, S. K., 1977: *Smoke, Dust and Haze.* John Wiley and Sons, 317 pp.

Fuchs, N. A., 1963: On the stationary charge distribution of aerosol particles in a bipolar ionic atmosphere. *Geofis. Pura. Appl.,* **56,** 185–193.

——, 1964: *The Mechanics of Aerosols.* Pergamon, 408 pp.

Gormley, P., and M. Kennedy, 1949: Diffusion from a stream flowing through a cylindrical tube. *Proc. Roy. Irish Acad.,* **52A,** 163 pp.

Hagen, D. E., and D. J. Alofs, 1983: Linear inversion method to obtain aerosol size distributions from measurements with a differential mobility analyzer. *Aerosol Sci. Technol.,* **2,** 465–475.

Hegg, D. A., R. J. Ferek, and P. V. Hobbs, 1993: Aerosol size distributions in the cloudy atmospheric boundary layer of the North Atlantic Ocean. *J. Geophys. Res.,* **98,** 8841–8846.

Hoppel, W. A., 1978: Determination of the aerosol size distribution from the mobility distribution of the charged fraction of aerosols. *J. Aerosol Sci.,* **9,** 41–54.

——, J. W. Fitzgerald, G. M. Frick, and R. E. Larson, 1990: Aerosol size distributions and optical properties found in the marine boundary layer over the Atlantic ocean. *J. Geophys. Res.,* **95,** 3559–3886.

Hudson, J. G., and A. D. Clarke, 1992: Aerosol and cloud condensation nuclei measurements in the Kuwait plume. *J. Geophys. Res.,* **97,** 14 533–14 536.

King, M. D., L. F. Radke, and P. V. Hobbs, 1993: Optical properties of marine stratocumulus clouds modified by ships. *J. Geophys. Res.,* **98,** 2729–2739.

Knutson, E. O., and K. T. Whitby, 1975: Aerosol classification by electrical mobility. *J. Aerosol Sci.,* **6,** p. 453.

McMurry, P. H., and D. J. Rader, 1985: Aerosol wall losses in electrically-charged chambers. *Aerosol Sci. Technol.,* **4,** 249–268.

Okuyama, K., Y. Kousaka, Y. Kida, and T. Yoshida, 1977: Turbulent coagulation of aerosols in a stirred tank. *J. Chem. Eng. Japan,* **10,** 142–147.

Quant, F. R., R. Caldow, G. J. Sem, and T. J. Addison, 1992: Performance of condensation particle counters with three continuous-flow designs. *J. Aerosol Sci.,* **23** (Suppl. 1), S405–S408.

Radke, L. F., J. A. Coakley, and M. D. King, 1989: Direct and remote sensing observations of the effects of ships on clouds. *Science,* **246,** 1146–1149.

——, C. A. Brock, J. H. Lyons, P. V. Hobbs, and R. C. Schnell, 1989: Aerosol and lidar measurements of hazes in mid-latitude and polar air masses. *Atmos. Environ.,* **23,** 2417–2430.

Russell, L. M., S. N. Pandis, and J. H. Seinfeld, 1994: Aerosol production and growth in the marine boundary layer. *J. Geophys. Res.,* **99,** 20 989–21 003.

——, R. C. Flagan, and J. H. Seinfeld, 1995: Asymmetric instrument response due to mixing effects in accelerated DMA-CPC measurements. *Aerosol Sci. Technol.,* **23,** 491–509.

Scheibel, H. G., and J. Porstendörfer, 1983: Generation of monodisperse Ag-aerosol and NaCl-aerosol with particle diameters between 2-nm and 300-nm. *J. Aerosol Sci.,* **14,** 113–126.

Seinfeld, J. H., 1986: *Atmospheric Chemistry and Physics of Air Pollution.* John Wiley and Sons, 738 pp.

Stolzenburg, M. R., and P. H. McMurry, 1991: An ultrafine aerosol condensation nucleus counter. *Aerosol Sci. Technol.,* **14,** 48–65.

Wang, S. C., and R. C. Flagan, 1990: Scanning electrical mobility spectrometer. *Aerosol Sci. Technol.,* **13,** 230–240.

Wiedensohler, A., 1988: An approximation of the bipolar charge-distribution for particles in the sub-micron size range. *J. Aerosol Sci.,* **19,** 387–389.

Winklmayr, W., G. P. Reischl, A. O. Lindner, and A. Berner, 1991: A new electromobility spectrometer for the measurement of aerosol size distributions in the size range from 1 to 1000 nm. *J. Aerosol Sci.,* **22,** 289–296.

Wolfenbarger, J. K., and J. H. Seinfeld, 1990: Inversion of aerosol size distribution data. *J. Aerosol Sci.,* **21,** 227–247.

Zhang, S. H., Y. Okutsu, L. M. Russell, R. C. Flagan, and J. H. Seinfeld, 1995: Radial differential mobility analyzer. *Aerosol. Sci. Technol.,* **23,** 357–372.